

LOW FRICTION LIQUID BEARING MEMS MICROMOTOR

Mei Lin Chan¹, Brian Yoxall¹, Hyunkyoo Park¹, Zhaoyi Kang², Igor Izyumin², Jeffrey Chou²,
Mischa M. Megens², Ming C. Wu², Bernhard E. Boser² and David A. Horsley¹

¹University of California, Davis, USA and ²University of California, Berkeley, USA

ABSTRACT

This paper examines the performance of rotating microdevices incorporating a liquid bearing to couple a rotating element to a fixed substrate. Liquid bearing technology promises to significantly improve the durability and lifetime of micromechanical motors. Here, the fluid is confined between the rotor and stator using surface patterning of a hydrophobic layer. Magnetic actuation of 10 mm diameter silicon rotor is used to characterize the liquid bearing motor at rotation rates up to 1800 rpm. Bearings with fluid thickness from 20-200 microns are characterized. A minimum torque of 0.15 $\mu\text{N}\cdot\text{m}$ is required to overcome static friction and initiate rotation. At rotation rates above 720 rpm, the rotor wobble is less than ± 1 mrad and the bearing exhibits viscous friction with a drag coefficient of 1.2×10^{-3} $\mu\text{N}\cdot\text{m}/\text{rpm}$.

INTRODUCTION

Surface tension and friction are dominant forces at small length scales. In this work, we exploit surface tension to overcome friction limitations in rotating microdevices by supporting a freely-rotating payload on a liquid rotary bearing. There are many instances of MEMS rotary motors in the literature. Examples include center-pinned wobble motors that have been actuated electrostatically [1, 2], ultrasonically [3] and magnetically [4] as well as motors incorporating micro-ball bearings [5]. A systemic problem with solid-solid contacts between the rotating parts and frame elements is friction. To minimize the effect of friction and wear in macroscale devices, fluid lubricating layers are often used to remove direct solid-solid contact. They take the form of externally pressurized gas-lubricated hydrodynamic bearings [6] and “air” bearings created through electrostatic or magnetic suspension [7, 8]. These support mechanisms often require complex fabrication processes with tight fabrication tolerances and complicated control schemes.

Here, instead of using pressurized fluid to provide the thrust for bearing support, surface tension between the thin liquid film and the patterned rotor and stator surfaces acts as the support mechanism. Although the liquid bearing principle has been demonstrated [9, 10] using electrowetting as the driving mechanism, little quantitative performance data or analytical modeling have been presented to date. Liquid bearing technology is wear resistant, capable of supporting both static and dynamic loads, and is self-centering with appropriate surface treatment. In this work, the liquid bearing is characterized via magnetic actuation of the rotor, enabling rotation rates over 1800 rpm. We also present experimental data on the load-bearing capacity,

viscous drag characteristics and wobble of the liquid bearing micromotor using water and ethylene glycol (EG) as the liquid layer in three different bearing geometries (disk, ring and full coverage).

PRINCIPLE & DESIGN

Figure 1 shows a schematic drawing of the liquid bearing rotor and the experimental setup used to power and characterize the liquid bearing. The surfaces of the rotor and stator are patterned with a 2 μm thick Cytop (Asahi) hydrophobic layer to define the bearing geometry. The contact angles of water and EG on the Cytop surface are ~ 99 and ~ 94 degrees respectively. The relatively high surface energy of glass and silicon allows the bearing liquid to wet the exposed surfaces, while the hydrophobic Cytop layer pins the bearing edges to a fixed location, as illustrated in Figure 2a.

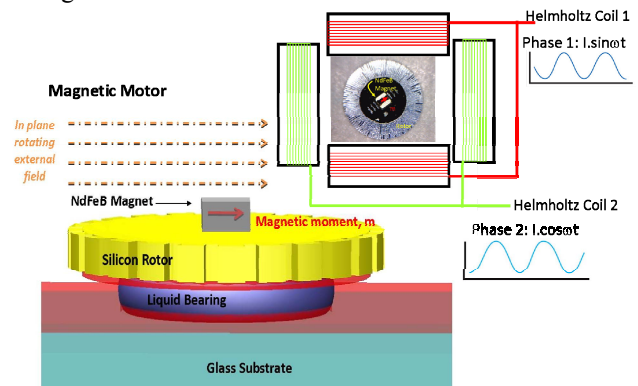


Figure 1: Schematic of the liquid bearing structure used to support a silicon rotor on a glass substrate. A NdFeB magnet mounted on the silicon rotor follows the rotating magnetic field generated by the two-axis Helmholtz coils.

Surface tension effects provide centering and load carrying capability. The bearing thickness, h , investigated in this work lies in the range between 20 to 200 μm thick, much smaller than the capillary length, l_c , of the liquids ($l_{c,H_2O} = 2.7$ mm, $l_{c,EG} = 2$ mm) in order to ensure that the rotor is dominated by the influence of surface tension.

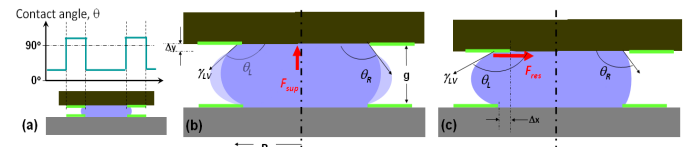


Figure 2: (a) Schematic of the cross section of the liquid bearing structure with variations in contact angle from non-wetting to wetting regions, forces acting on the rotor due to surface tension (b) to support and (c) center the rotor.

For motion in a direction normal to the rotor face, as illustrated in Figure 2b, the “piston” direction, a lifting force F_{sup} results from both Laplace pressure and surface tension:

$$F_{sup} = \frac{\pi R^2 \gamma_{LV}}{g} (\cos \theta_R + \cos \theta_L) + 2\pi R \gamma_{LV} \sin \theta_{R,L} \quad (1)$$

where γ_{LV} is the fluid surface tension, g is the bearing thickness, R is the bearing radius, θ is the contact angle and the subscripts R and L denote right and left contact angle.

For transverse motion parallel to the rotor face (see Figure 2c), the restoring force due to surface tension is:

$$F_{res} = 2(\gamma_{LV} \cos \theta_R - \gamma_{LV} \cos \theta_L) \quad (2)$$

By selecting a suitable liquid with low viscosity, μ ($\mu_{H2O} = 1$ mPa·s, $\mu_{EG} = 16.1$ mPa·s), the rotor can operate in a low friction domain. Similarly, the surface tension, γ_{LV} ($\gamma_{LV, H2O} = 72.8$ mJ/m², $\gamma_{LV, EG} = 47.7$ mJ/m²), determines the load-carrying capacity of the bearing. The friction characteristics of the liquid bearing are a function of fluid thickness, radius, curvature of the bearing edge, and roughness of the bearing boundary. In this work, we will focus on the influence of bearing thickness and geometry on the operating friction and start-up torque to evaluate the performance of the liquid bearings.

Fabrication

The fabrication process for both rotor and stator is detailed in Figure 3. The stator is fabricated from a glass substrate while the rotor is 10 mm diameter disk made from a 300 μ m thick silicon wafer. A photoresist liftoff process is used to pattern the Cytop layer on both the stator and rotor (see Figure 3a-d). The patterned Cytop layer serves as the hydrophobic confinement surface that defines the shape and size of the liquid bearing.

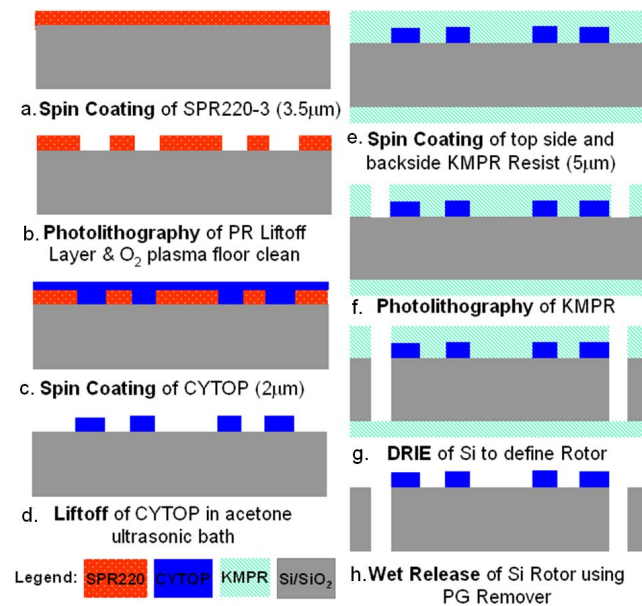


Figure 3: Schematic of the microfabrication process for both glass stator and Si rotor. The stator’s fabrication stops at step d, while the Si rotor continues through step h.

The uncoated glass/silicon area serves as the anchor for the liquid bearing. In the case of the silicon rotor, more processing steps are required (Figure 3e-h). A thick photoresist (KMPR 1005, MicroChem) is used to define the rotor pattern for the DRIE through-wafer etch, and a final wet release step frees the rotor for subsequent assembly.

A 1.5 mm Neodymium (NdFeB) magnet cube with magnetic moment, m , of 4.1×10^{-3} A·m² is centered and mounted on top of the rotor. The mass moment of inertia of the rotor is 6.86×10^{-10} kgm² and 6.96×10^{-10} kgm² with and without the magnet, respectively; while the total weight of the rotor-magnet structure is ~ 90 mg. Figure 4 shows the bottom view of a complete (stator-liquid bearing-rotor) device assembled using a vacuum pick-and-place technique. The bottom view is taken through the glass stator focusing on the liquid bearing and the bottom of the rotor. This view highlights the single droplet liquid bearing structure with 10 μ l of liquid confined within the 6 mm diameter annular patterned Cytop layer.

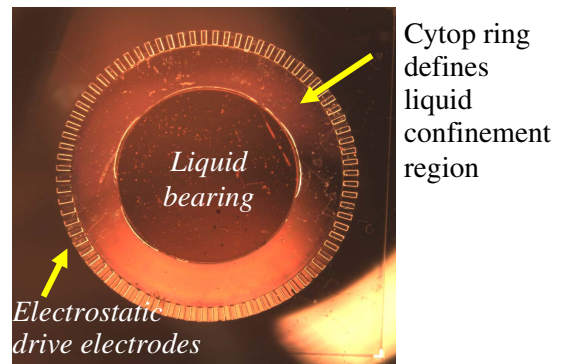


Figure 4: Optical micrograph through the glass stator showing the confinement of the liquid within the patterned Cytop ring. The diameter of the liquid bearing is 6 mm.

Magnetic Drive Mechanism

The mechanical performance of the liquid bearing micromotor was characterized using magnetic actuation where two orthogonal pairs of Helmholtz coils are used to spin the rotor. The coil pairs are driven 90 degrees out of phase, at matched amplitudes, to create a rotating magnetic field with uniform magnitude in the range of $B = 1$ mT. The frequency of the coil signal, Ω , determines the motor rotation rate while the field amplitude provides control over the applied torque, as detailed below.

RESULTS AND DISCUSSION

Torque Measurements

Table 1 highlights the three different geometries investigated. For both the ring and disk bearings, the shape of the bearings is confined by the patterned Cytop layer. In the case of the full bearing design, the liquid is trapped under the rotor and within a 300 μ m wide circumferential gap around the rotor periphery.

The drag induced by the liquid bearing during rotation

is an important comparison metric for evaluating the performance of the bearing relative to prior work. The total drag of the bearing, τ_b , is speed dependent and the bearing exhibits both viscous and static friction (stiction). The applied magnetic torque, $\tau_{applied}$, provided by the rotating magnetic field, B , on the rotor with magnetic moment, m , is a function of the phase angle, ϕ , between B and m as defined in equation 3.

$$\tau_{applied} = \vec{m} \times \vec{B} = |m||B|\sin\phi \quad (3)$$

Table 1: Table of the varying liquid bearing geometries used in the measurements.

Bearing Design	Disk Bearing	Ring Bearing	Full Bearing
Top View of Bearing			
Cross Section View of Bearing			
Rotor Radius [mm]	5	5	5
Bearing Radius [mm]	3	Inner = 1.5, Outer = 3.5	5

Start-up Torque Requirement

Startup torque, τ_s , is defined as the minimum $\tau_{applied}$ for the rotor to begin spinning. Figure 5 shows experimental measurement of τ_s for different bearings geometries, fluid thicknesses and viscosities. The data show an exponential dependence on the fluid thickness, g . Moreover, the startup torque for the EG bearing is only slightly larger than that for H₂O, indicating that that fluid viscosity does not play an important role at slow rotation rates.

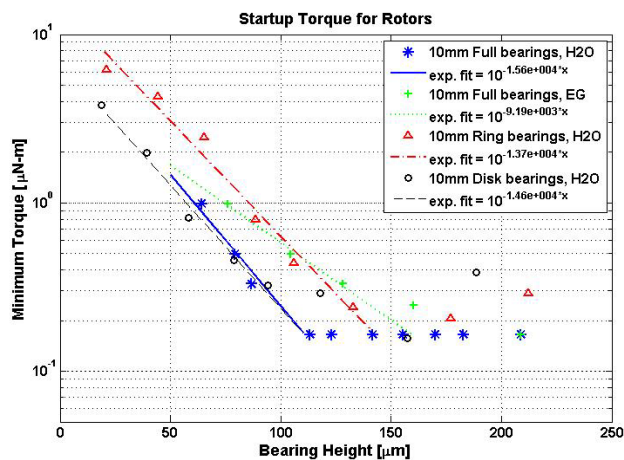


Figure 5: Experimental data showing the trend of the starting torque with respect to varying bearing thickness and bearing geometries.

In the case of both ring and disk bearings, as the thickness of the bearing increases the bearing becomes less stable in tip/tilt. The edges of the tipping rotor contact the stator, resulting additional stiction and an increased startup

torque. This tip/tilt instability is not apparent in the full coverage bearing, allowing the fluid bearing to be thicker. The start-up torque for the full bearing remains constant at 0.15 $\mu\text{N}\cdot\text{m}$ for $g > 120 \mu\text{m}$.

Viscous Friction Drag

For fluid bearings thicker than 100 μm , startup torque is small and τ_b is dominated by viscous friction, $\tau_v = b\Omega$, where Ω is rotation rate and b is the viscous drag coefficient. When the friction is less than $\tau_{max} = \max(\tau_{applied}) = |m||B|$, increasing Ω increases drag and the phase angle, ϕ , approaches 90°. The critical rate of rotation occurs when $\tau_b = \tau_{max}$, above which the rotor oscillates at the excitation frequency but does not spin. Figure 6 shows the maximum rotation rate depends linearly on both the liquid bearing thickness and the applied torque, consistent with the viscous friction model in equation 4, where g is the bearing thickness, μ is fluid viscosity, and R is the bearing radius.

$$b = \frac{\mu\pi R^4}{2g} \quad (4)$$

The mean viscous drag coefficient calculated experimentally as $b = |m||B|/\Omega_{max}$ for disk bearing designs from 110-150 μm thick, is $1.2 \times 10^{-3} \mu\text{N}\cdot\text{m}/\text{rpm}$ which is 20% higher than equation 4 predicts using known values for the fluid viscosities. This result can be attributed to measurement uncertainty in the bearing thickness during torque measurements. For an input torque of 1.6 $\mu\text{N}\cdot\text{m}$, the maximum rotation rate as a function of the bearing thickness is calculated to be 0.225 rps/ μm for the disk shaped H₂O bearing.

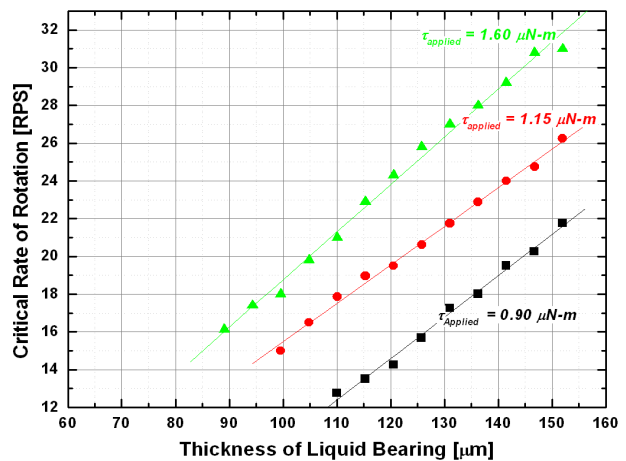


Figure 6: Experimental data showing the maximum rotation rate above which the rotor fails to follow the magnetic field. Measurements were conducted over different bearing thicknesses and magnetic torque levels to identify the parameters of a viscous friction model.

Maximum Rotation Rate

In Figure 6, for liquid bearings at $\sim 145\text{-}150 \mu\text{m}$ thickness, with a $\tau_{applied}$ of 1.60 $\mu\text{N}\cdot\text{m}$, the maximum rotation rate was $\Omega_{max} = 30 \text{ Hz}$, or 1800 rpm. Figure 7

shows images of the rotor at rest, during spin up and at a constant rate of rotation of 1800 rpm. The rotors can be actuated in the upright mode as well as the inverted mode.

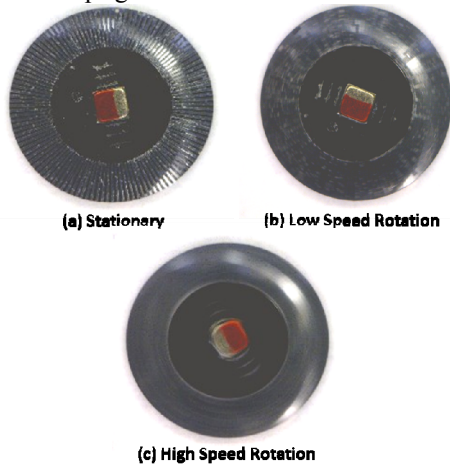


Figure 7: Three video capture frames showing the magnetically actuated motor (a) at rest, (b) undergoing low speed rotation, and (c) rotating at a maximum rotation rate of 1800 rpm.

Wobble

A second performance characteristic of bearings is the angular displacement of the rotor normal axis relative to the stator normal axis, referred to as rotor wobble. There are various contributions to the dynamic track error on a spinning liquid bearing rotor: 1) eccentricity error due to misalignment of bearing with respect to rotor, 2) cogging due to surface defects at the edge of the bearing and 3) error due to the mounting of the magnet on the rotor. The dominant error is in the misaligned magnet with respect to that of the silicon rotor, which already manifests itself in the form of significant static tilt of the rotor.

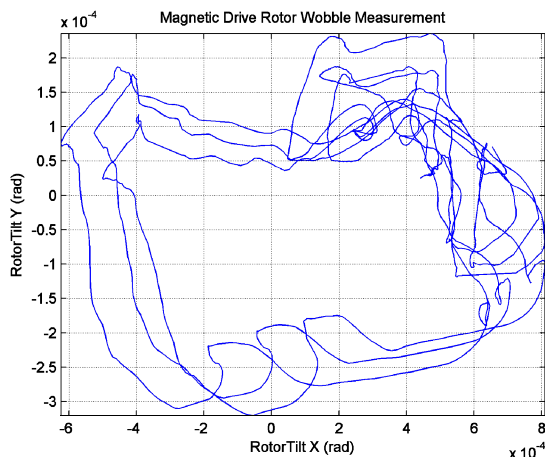


Figure 8: Dynamic trajectory of the full bearing rotor spinning at a rotation rate of 500 rpm.

To measure wobble in our system, a laser beam is reflected off the rotor surface at $\sim 45^\circ$ to the stator normal into a 2-axis PSD. The repeatable wobble trajectory of a full liquid bearing rotor spinning at speed of ~ 500 rpm is plotted in Figure 8 and shows wobble at less than ± 1 mrad.

For both ring and disk bearing, the wobble is significant at all speeds. However, in the case of the full bearing, the wobble is only significant at low speeds. At high spin rates, hydrodynamic force created by the circumferential fluid film help to center the bearing and maintain uniform gap between the rotor and its edges to prevent solid contact and allow for smoother free rotation.

CONCLUSIONS

We have demonstrated a novel liquid bearing and characterized several important physical parameters governing the performance of liquid bearing rotating microdevices. The minimum torque required to spin the rotor is $\sim 0.15 \mu\text{N}\cdot\text{m}$, and rotation rates up to 1800 rpm were demonstrated. The drag performance of the disk-type liquid bearing using H_2O as the fluid is approximately 15 times lower than that demonstrated in a micro-ball bearing supported rotor. Torque measurements conducted at speeds greater than 720 rpm were consistent with a viscous friction model, with the drag constant showing an inverse dependence on the fluid thickness. The start-up torque required to initiate rotation was also shown to diminish with increasing fluid thickness up to $g \sim 120 \mu\text{m}$. However the physical mechanism determining the start-up torque is not yet well-understood.

ACKNOWLEDGEMENT

This work is supported by DARPA under grant W31P4Q-10-1-0002. The authors would like to thank the support of UC Davis Nanofabrication Center.

REFERENCES

- [1] L. S. Fan, Y. C. Tai, and R. S. Muller, "Sensors and Actuators", vol. 20, no. 1-2, pp. 41-47, Nov, 1989.
- [2] M. Mehregany, S. F. Bart, L. S. Tavrow *et al.*, "Sensors and Actuators a-Physical", vol. 21, no. 1-3, pp. 173-179, Feb, 1990.
- [3] V. Kaajakari, and A. Lal, "Sensors and Actuators a-Physical", vol. 137, no. 1, pp. 120-128, Jun, 2007.
- [4] C. H. Ahn, Y. J. Kim, and M. G. Allen, "Journal of Microelectromechanical Systems", vol. 2, no. 4, pp. 165-173, December, 1993.
- [5] N. Ghalichechian, A. Modafe, M. I. Beyaz *et al.*, "Journal of Microelectromechanical Systems", vol. 17, no. 3, pp. 632-642, Jun, 2008.
- [6] L. G. Frechette, S. A. Jacobson, K. S. Breuer *et al.*, "Journal of Microelectromechanical Systems", vol. 14, no. 1, pp. 141-152, Feb, 2005.
- [7] S. Kumar, D. Cho, and W. N. Carr, "Journal of Microelectromechanical Systems", vol. 1, no. 1, pp. 23-30, March, 1992.
- [8] X. S. Wu, W. Y. Chen, X. L. Zhao *et al.*, "Electronics Letters", vol. 40, no. 16, pp. 996-997, Aug, 2004.
- [9] A. Takei, N. Binh-Khiem, E. Iwase *et al.*, "MEMS '08, Tucson, AZ, 2008, pp. 42-45.
- [10] A. Kajiwarra, K. Suzuki, H. Miura *et al.*, "Research Reports of Kogakuin University", no. 101, pp. 25-30, October, 2006.